

Cite this: *Energy Environ. Sci.*, 2025, 18, 9018

# Interfacial energy storage in aqueous zinc-ion batteries

Yuhang Dai,<sup>†\*</sup> Chengyi Zhang,<sup>†</sup> Xinyu Zhang,<sup>b</sup> Peie Jiang,<sup>ab</sup> Jie Chen,<sup>id b</sup> Wei Zong,<sup>id a</sup> Sicheng Zheng,<sup>b</sup> Xuan Gao,<sup>\*b</sup> Thomas J. Macdonald<sup>d</sup> and Guanjie He<sup>id \*b</sup>

Aqueous zinc-ion batteries (AZIBs) are attractive for large-scale energy storage due to their intrinsic safety, low cost, and environmental compatibility. However, the high charge-to-radius ( $q/r$ ) ratio of  $Zn^{2+}$  leads to strong solvation and sluggish solid-state diffusion, which hinder efficient charge transport across solid–solid and solid–liquid interfaces. These limitations reduce both cycling stability and rate performances. In this review, we summarize interfacial transport regulation strategies, including solid–solid interfacial modulation via electrostatic fields, interfacial bonding, and ion–electron decoupling to enhance solid-state  $Zn^{2+}$  mobility. We further discuss solid–liquid interfacial desolvation regulation including water activity control, solvation structure tuning, and selective ion channels to mitigate desolvation barriers. We also describe emerging mechanisms involving water dissociation at interfaces, where protons and hydroxide ions act as alternative charge carriers. These unconventional pathways can complement or even outperform traditional  $Zn^{2+}$  intercalation. Collectively, these interfacial strategies not only accelerate  $Zn^{2+}$  transport but also introduce new electrochemical phenomena that boost capacity and rate performances of AZIBs. Advancing the deliberate design and mechanistic understanding of such interfacial processes will be essential to unlocking the full potential of next-generation AZIBs.

Received 2nd July 2025,  
Accepted 4th September 2025

DOI: 10.1039/d5ee03741g

rsc.li/ees

## Broader context

The development of safe, long-lasting, and cost-effective energy storage technologies is essential for the widespread integration of renewable energy. Aqueous zinc-ion batteries (AZIBs) have attracted increasing interests due to their intrinsic safety, non-flammable water-based electrolytes, and the low cost and abundance of their electrode materials. These advantages make AZIBs promising for grid-scale storage, peak-shaving, and fast-charging applications. However, their practical performance remains limited by interfacial challenges, as  $Zn^{2+}$  ions interact strongly with both solid electrodes and water molecules in the solvation shell. Problems such as dendrite growth, parasitic water decomposition reactions, and sluggish ion transport have not yet been fully resolved. While advances in material and electrolyte design have yielded significant improvements, interfacial regulation is increasingly recognized as a key factor that directly governs  $Zn^{2+}$  migration and overall electrochemical performance. Recent studies suggest that rationally engineered interfaces can not only suppress degradation but also boost capacity and charging rates. Notably, emerging studies revealed that water dissociation products, such as protons and hydroxide ions, can actively participate in charge storage, enabling unconventional mechanisms beyond  $Zn^{2+}$  insertion. Continued advances in understanding and controlling interfacial processes will be essential for realizing the full potential of AZIBs in practical energy storage systems.

## 1. Introduction

Since 2012, aqueous zinc-ion batteries (AZIBs) have been extensively investigated as promising candidates for large-scale energy storage because they combine cost-effectiveness and environmental sustainability.<sup>1–4</sup> In addition, the use of water-based electrolytes eliminates fire risks and enables safer operation compared to conventional lithium-ion batteries.<sup>5</sup> These advantages render AZIBs attractive for grid balancing, backup storage, and fast-charging applications. They are especially suitable for scenarios where safety, long cycle life, and high power density are critical.<sup>6</sup>

<sup>a</sup> Department of Engineering Science, University of Oxford, Oxford OX1 3PJ, UK. E-mail: yuhang.dai@eng.ox.ac.uk

<sup>b</sup> Christopher Ingold Laboratory, Department of Chemistry, University College London, London WC1H 0AJ, UK. E-mail: xuan.gao.21@ucl.ac.uk, g.he@ucl.ac.uk

<sup>c</sup> School of Chemical Sciences, The University of Auckland, Auckland 1010, New Zealand

<sup>d</sup> Department of Electronic and Electrical Engineering, University College London, London WC1E 7JE, UK

<sup>†</sup> These authors contribute equally.



Despite these advantages, the practical deployment of AZIBs remains hindered by intrinsic scientific challenges. The key issue stems from the high charge density and small ionic radius of  $\text{Zn}^{2+}$  (+2, 0.74 Å),<sup>7</sup> compared to  $\text{Li}^+$  (+1, 0.76 Å),<sup>8</sup> resulting in much stronger electrostatic interactions with host lattices and coordinated water molecules in its solvation shell. Consequently,  $\text{Zn}^{2+}$  experiences sluggish solid-state diffusion and a high desolvation (removal of coordinated solvent molecules from ions prior to insertion into the host material) penalty at electrode–electrolyte interfaces. These limitations induce uneven Zn plating, dendrite formation, parasitic side reactions such as hydrogen evolution, and structural degradation of cathode materials through dissolution or distortion, ultimately impairing cycling stability and overall efficiency.

To tackle these challenges, extensive efforts have been devoted to both electrode and electrolyte design. On the cathode side, phase engineering, pre-intercalation strategies,<sup>9</sup> and anion redox mechanisms<sup>10</sup> have been explored to stabilize host structures and promote  $\text{Zn}^{2+}$  storage. Electrolyte engineering has primarily targeted the bulk solvation environment of  $\text{Zn}^{2+}$  through highly concentrated electrolytes (water-in-salt systems<sup>11</sup>), eutectic formulations,<sup>12</sup> solvation structure modulation *via* donor number adjustments,<sup>13</sup> and diverse additives, whose functional groups can critically modulate solvation structure and interfacial chemistry to mitigate side reactions.<sup>14–16</sup> For zinc metal anodes, crystallographic orientation control has been employed to suppress dendrite growth and improve reversibility.<sup>17</sup>

In parallel, interfacial regulation has increasingly emerged as a systematic strategy to address multiple bottlenecks that fundamentally govern  $\text{Zn}^{2+}$  transport and reaction kinetics. Integrated with the European initiative Battery 2030+, which underscores the importance of interface control for future battery innovation, recent interfacial designs in AZIBs encompass solid–solid composite architectures within cathodes,<sup>18</sup> protective interphases at electrode–electrolyte interfaces,<sup>19</sup> and Zn anode modifications such as cation-adsorbed shielding layers.<sup>20</sup> These approaches collectively enhance  $\text{Zn}^{2+}$  mobility, facilitate desolvation, suppress parasitic reactions, and enable additional reaction pathways related to interfacial water dissociation, thereby improving energy density and cycling stability especially under high-rate cycling conditions.

Herein, recent advances in interfacial regulation of  $\text{Zn}^{2+}$  transport are systematically summarized. We specifically focus on interfacial phenomena that govern charge storage and reversibility, rather than providing a comprehensive survey of all aspects of AZIBs such as Zn anode morphology or full-cell engineering. In contrast to previous reviews that largely emphasize Zn anodes or electrolyte design, our work complements them by highlighting cathode-side interfacial regulation.<sup>21–26</sup> Within this scope, we integrate mechanistic insights to uncover emerging interfacial processes in which water dissociation products directly participate in charge storage. These insights reveal unconventional capacity gains and exceptionally fast kinetics. A deeper mechanistic understanding of interfacial  $\text{Zn}^{2+}$  transport is expected to inform novel design principles for next-generation high-performance aqueous zinc-ion batteries.

## 2. Regulation of $\text{Zn}^{2+}$ transport at solid–solid interfaces

The design of solid–solid interfaces plays a pivotal role in addressing ion transport limitations within electrode materials. The strong electrostatic interaction between  $\text{Zn}^{2+}$  and host lattices often results in sluggish solid-state diffusion, which becomes particularly pronounced under practical high-loading conditions. By rationally engineering heterointerfaces within composite materials, it is possible to modulate local electrostatic fields, establish interfacial chemical bonding, and spatially decouple ion and electron transport pathways, thereby enabling more efficient  $\text{Zn}^{2+}$  migration across solid–solid interfaces.

### 2.1 Electrostatic modulation of $\text{Zn}^{2+}$ migration

Electrostatic regulation at solid–solid heterointerfaces has been demonstrated as an effective strategy to accelerate  $\text{Zn}^{2+}$  migration by lowering the diffusion energy barrier. In particular, constructing built-in electric fields reshapes the local charge distribution, thereby enhancing  $\text{Zn}^{2+}$  adsorption and facilitating ion transport. A representative example is the  $\text{H}_2\text{V}_3\text{O}_8$ –MXene heterostructure, where charge redistribution across the interface induces a strong internal electric field that promotes  $\text{Zn}^{2+}$  migration (Fig. 1(a)–(c)).<sup>27</sup> Density functional theory (DFT) calculations revealed that the  $\text{Zn}^{2+}$  migration barrier was significantly reduced from 3.4 eV in pure  $\text{H}_2\text{V}_3\text{O}_8$  to 1.3 eV at the interface, accompanied by distinct charge transfer and increased electron density near the Fermi level. This combination improves both electronic conductivity and  $\text{Zn}^{2+}$  diffusion kinetics.

Similar electrostatic modulation effects have been reported in various heterointerface systems. For instance, the  $\text{V}_2\text{C}$ – $\text{V}_2\text{O}_5$  heterostructure forms a highly polarized interface that strengthens the local electric field, enhancing  $\text{Zn}^{2+}$  adsorption and reducing migration barriers.<sup>28</sup> Likewise, the Cu-HHTP–MXene (HHTP = 2, 3,6,7,10,11-hexahydroxytriphenylene) hybrid forms extended two-dimensional channels with open coordination environments that facilitate  $\text{Zn}^{2+}$  transport under the influence of interfacial electric fields.<sup>29</sup> In another example, MnO–nitrogen-doped graphene aerogel (NGA) composites leverage interfacial charge redistribution from MnO–NGA interactions to promote  $\text{Zn}^{2+}$  migration.<sup>30</sup> Interfacial polarization has also been exploited in  $\text{MoS}_2$ –MXene heterostructures, where strong interlayer interactions contribute to reduced  $\text{Zn}^{2+}$  diffusion barrier.<sup>31</sup> In another case, poly(3,4-ethylenedioxythiophene) (PEDOT) modified  $\text{V}_2\text{O}_5$  nanosheets exhibit improved  $\text{Zn}^{2+}$  storage kinetics by facilitating capacitive behaviors through an enhanced surface charge density.<sup>32</sup>

Collectively, these studies demonstrate that engineering built-in electric fields at heterointerfaces provides an efficient means to regulate  $\text{Zn}^{2+}$  adsorption and migration, offering improved charge transfer and fast ion transport pathways.

### 2.2 Interfacial chemical bonding pathways

In addition to electrostatic effects, constructing interfacial chemical bonds offers another effective route to regulate  $\text{Zn}^{2+}$  migration. Chemical bonding at the interface serves as anchor points that stabilize the inserted  $\text{Zn}^{2+}$ , lower diffusion barriers,





**Fig. 1** Solid–solid interfacial regulation of Zn<sup>2+</sup> transport through electrostatic fields and chemical bonding. (a) DFT-calculated Zn<sup>2+</sup> adsorption energies on H<sub>2</sub>V<sub>3</sub>O<sub>8</sub>–MXene interface with various configurations. (b) Charge density difference showing interfacial charge redistribution. (c) Zn<sup>2+</sup> migration barriers on pristine H<sub>2</sub>V<sub>3</sub>O<sub>8</sub> and H<sub>2</sub>V<sub>3</sub>O<sub>8</sub>–MXene interface. Reproduced from ref. 27. Copyright (2022), with permission from Elsevier. (d) Schematic of interfacial activation and Zn<sup>2+</sup> transport pathways enabled by V–O–Ti–C bonding. (e) Dynamic evolution of V–O–Ti bonds during cycling, facilitating reversible Zn<sup>2+</sup> insertion. Reproduced from ref. 33. Copyright (2023), with permission from Wiley-VCH.

and create directional pathways for ion movement. A representative example is the V<sub>5</sub>O<sub>12</sub>–Ti<sub>3</sub>C<sub>2</sub> heterostructure, where dynamic V–O–Ti bonds form at the interface and actively participate during cycling (Fig. 1(d) and (e)).<sup>33</sup> These bonds undergo reversible breaking and reformation as Zn<sup>2+</sup> inserts and extracts, buffering volume changes while maintaining structural integrity and delivering high capacity with excellent stability.

Various other heterostructures have implemented similar bonding strategies to regulate Zn<sup>2+</sup> transport. Specifically, in VO<sub>2</sub>@Co–N–C composites, atomically dispersed Co–N coordination centers form Co–O–V bonds with VO<sub>2</sub>, which modulate local charge distribution and facilitate Zn<sup>2+</sup> adsorption and directional diffusion.<sup>34</sup> Similarly, the V<sub>2</sub>O<sub>5</sub>@NC system introduces nitrogen-doped carbon interfaces that generate V–O–C bonds, guiding Zn<sup>2+</sup> migration while stabilizing structural frameworks.<sup>35</sup> In another case, the IC@MnO<sub>2</sub> material introduces positively charged interstitial carbon (IC) into the MnO<sub>2</sub> lattice, leading to the formation of Mn–O–C bonds. These interfacial bonds facilitate simultaneous Zn<sup>2+</sup> and H<sup>+</sup> intercalation, improving both capacity and reversibility.<sup>36</sup> In addition to these examples, the V<sub>2</sub>C–V<sub>2</sub>O<sub>5</sub> and Cu–HHTP–MXene heterostructures also exhibit interfacial bonding features that contribute to the Zn<sup>2+</sup> transport enhancement alongside their electrostatic effects.<sup>28,29</sup>

These interfacial bonding configurations offer tunable energy landscapes that enable fast, directional Zn<sup>2+</sup> migration with suppressed structural degradation, providing an attractive pathway for high-rate AZIBs.

### 2.3 Ion–electron decoupling at composite interfaces

Beyond controlling ion migration barriers, spatial decoupling of electron and Zn<sup>2+</sup> transport (separating the pathways of electron and ion transport), a concept originating from lithium-ion systems, provides a distinct strategy to achieve both high capacity and rapid charge storage.<sup>37</sup> This “job-sharing” mechanism creates heterointerfaces where Zn<sup>2+</sup> and electrons are stored and transported in separate yet adjacent domains. A typical example is the VO<sub>x</sub>–reduced graphene oxide (rGO) composite,<sup>38</sup> where Zn<sup>2+</sup> ions are predominantly stored in regions where sub-nanometer VO<sub>x</sub> clusters are loaded onto rGO, as shown in the scanning transmission electron microscopy (STEM) image (Fig. 2(a)). This suggests that ion storage sites are jointly defined by both VO<sub>x</sub> and rGO. Mechanistically, interfacial V–O–C bonds in the pristine state convert into V–O–V bonds during Zn<sup>2+</sup> insertion, as confirmed by Raman spectroscopy (Fig. 2(c)), indicating Zn<sup>2+</sup>-induced interfacial bond reconstruction. Electron energy loss spectroscopy (EELS) further shows an increase in the vanadium valence state during charging (Fig. 2(d)), confirming redox activity localized at VO<sub>x</sub> sites. Meanwhile, enhanced π–π\* shake-up signals observed in the rGO (Fig. 2(e)) indicate electron delocalization through the conductive carbon network, corroborating the spatial separation of electron and ion pathways.

Together, these findings reveal a decoupled transport mechanism in which Zn<sup>2+</sup> ions are stored *via* redox reactions on VO<sub>x</sub>, while electrons are conducted through rGO (Fig. 2(b)). Galvanostatic intermittent titration technique (GITT) measurements in this work further reveal that the Zn<sup>2+</sup> diffusion





**Fig. 2** Solid–solid interfacial regulation of Zn<sup>2+</sup> transport through electron–ion decoupling. (a) STEM image of VO<sub>x</sub>–rGO showing VO<sub>x</sub> clusters and Zn<sup>2+</sup> storage at the interface. (b) Schematic of spatially separated Zn<sup>2+</sup> storage and electron conduction enabling pseudocapacitive behavior. (c) Raman spectra tracking V–O–C bond changes upon cycling. (d) EELS analysis of vanadium valence evolution. (e) C 1s XPS spectra showing V–O–C bonding and π–π\* signals. Reproduced from ref. 38. Copyright (2023), with permission from Wiley-VCH.

coefficient of VO<sub>x</sub>–rGO is over two orders of magnitude higher than that of bulk VO<sub>2</sub>, corroborating the markedly accelerated ion transport enabled by the decoupled electron/ion pathways. This system delivers a high specific capacity of 443 mAh g<sup>-1</sup> at 100 mA g<sup>-1</sup> and maintains excellent rate capability, retaining 174.4 mAh g<sup>-1</sup> at 100 A g<sup>-1</sup>. Moreover, the charge storage process is governed by pseudocapacitive (surface-controlled fast charge storage process) behavior, and such an interfacial Zn<sup>2+</sup> storage strategy sustains high-rate performance even at practical mass loadings up to 12.72 mg cm<sup>-2</sup> (3.67 mAh cm<sup>-2</sup> at 1.27 mA cm<sup>-2</sup>). In addition, its facile synthesis process offers promising scalability for large-scale electrode fabrication.

The job-sharing principle has been extensively explored in VO<sub>x</sub>–graphene oxide (GO) composites by Liu *et al.*, where hydrogen-bonded N·H–O interfaces further enhance charge separation and ion storage efficiency.<sup>39</sup> In this system, Zn<sup>2+</sup> ions are selectively adsorbed onto the VO<sub>x</sub> domains, while electrons are delocalized within the GO sheets, collectively establishing interfacial intercalation pseudocapacitance characterized by rapid kinetics and minimal vanadium redox fluctuation. Quantitative analyses revealed that more than 90% of Zn<sup>2+</sup> storage occurred at the interface, while bulk contributions remained negligible. The hydrogen-bonded interface also imparted a self-healing capability, enabling stable long-term cycling even at high mass loadings.

These interface-governed job-sharing designs offer a unique pathway to simultaneously enhance Zn<sup>2+</sup> diffusion, electron conductivity, and structural stability, thereby enabling AZIBs with both high capacity and fast charge–discharge characteristics.

Despite their advantages, these solid–solid interfacial strategies also present trade-offs. Electrostatic field designs often require complex heterostructures, interfacial bonding may hinder Zn<sup>2+</sup> transport if overly strong, and ion–electron decoupling relies on added conductive frameworks that can increase material complexity. Balancing structural benefits with synthetic feasibility remains essential for their practical deployment.

### 3. Regulation of desolvation at solid–liquid interfaces

#### 3.1 Cathode–electrolyte interfacial desolvation

The desolvation of hydrated Zn<sup>2+</sup> prior to intercalation into cathode materials strongly influences interfacial kinetics. Regulating interfacial environments has enabled multiple strategies to accelerate desolvation while maintaining interfacial stability.



**3.1.1 Water masking strategy.** Water masking represents an effective strategy to lower the desolvation barrier at the cathode–electrolyte interface by modulating the  $\text{Zn}^{2+}$  solvation structure. By introducing tailored interfacial layers that selectively repel or reorient water molecules,  $\text{Zn}^{2+}$  can approach the host material with fewer coordinated water molecules, facilitating faster intercalation kinetics.

One representative example is the work by Zhong *et al.*, who introduced an interfacial desolvation enhancer (IDE) molecule that self-assembles as a monolayer on hydrated vanadium oxide cathodes.<sup>40</sup> As shown in Fig. 3(a)–(c), molecular dynamics simulations and coordination number analyses reveal that IDE molecules preferentially adsorb on the cathode surface, displacing interfacial  $\text{H}_2\text{O}$  molecules and reducing the number of coordinated water molecules in the  $\text{Zn}^{2+}$  solvation shell—from five in the control to four in the IDE20 system.

Importantly, IDE does not participate in the  $\text{Zn}^{2+}$  solvation shell, thereby minimizing its influence on ion size and preserving transport kinetics. This selective interfacial masking weakens  $\text{Zn}^{2+}$ – $\text{H}_2\text{O}$  interactions and lowers the desolvation energy, resulting in enhanced rate capability and cycling stability. The IDE-coated cathodes maintain structural integrity and deliver stable performances even under high current densities.

Other studies have further illustrated water masking approaches. Gou *et al.* constructed a hydrophobic PEDOT layer inspired by biological membranes on  $\text{MnO}_2$  cathodes, which reduced water access and promoted  $\text{Zn}^{2+}$  desolvation.<sup>41</sup> Furthermore, Ding *et al.* utilized F-coordination to regulate local water activity and enhance desolvation on  $\text{MnO}_2$  surfaces.<sup>42</sup> These results demonstrate the broad applicability of water masking strategies to improve cathode interfacial kinetics in AZIBs.



**Fig. 3** Representative cathode–electrolyte interfacial desolvation regulation strategies in AZIBs. (a), (b) Radial distribution function and coordination number of  $\text{Zn}^{2+}$  with  $\text{OTf}^-$  and  $\text{H}_2\text{O}$  in 2 M  $\text{Zn}(\text{OTf})_2$  electrolyte (a) and 2 M  $\text{Zn}(\text{OTf})_2$  with 20 mM isosorbide dimethyl ether (IDE) (b). (c) Snapshot of IDE monolayer on hydrated VOH surface showing distributions of  $\text{H}_2\text{O}$ ,  $\text{OTf}^-$ , and  $\text{Zn}^{2+}$ . Reproduced from ref. 40 Copyright (2024), with permission from Royal Society of Chemistry. (d) Energy barriers for the desolvation process of  $[\text{Zn}(\text{H}_2\text{O})_5]^{2+}(\text{CF}_3\text{SO}_3)^-$  on  $\text{TiS}_2$  and  $\text{TiS}_2\text{-TiO}_2$  surfaces. (e), (f) Mass change per mole of electron for  $\text{TiS}_2\text{-TiO}_2$  electrode (TSO-2) (e) and pure  $\text{TiS}_2$  electrode (TS) (f) electrodes during cyclic voltammetry (CV) scans. Reproduced from ref. 43 Copyright (2025), with permission from Wiley-VCH. (g) Mean square displacement of different ions in  $\text{Zn}_x(\text{OTf})_y(\text{OH})_{2x-y}\cdot n\text{H}_2\text{O}$  (ZnOTf-LDH) from *ab initio* molecular dynamics (AIMD) simulations. (h) Adsorption energy of  $\text{Zn}^{2+}$  and  $\text{H}_2\text{O}$  within the channel of ZnOTf-LDH. (i) CV curves of  $\text{V}_6\text{O}_{13}$  and  $\text{V}_6\text{O}_{13}$  coated with ZnOTf-LDH at 0.1  $\text{mV s}^{-1}$ . Reproduced from ref. 44 under the Creative Commons CC BY license.



**3.1.2 Built-in electric field assisted desolvation.** Beyond water masking, engineering internal electric fields at the cathode interface offers another pathway to accelerate  $\text{Zn}^{2+}$  desolvation. Localized electric fields can polarize incoming solvated  $\text{Zn}^{2+}$  ions, promoting partial removal of coordinated water molecules prior to  $\text{Zn}^{2+}$  intercalation.

Chen *et al.*<sup>43</sup> constructed a  $\text{TiS}_2$ - $\text{TiO}_2$  heterostructure that induces a built-in electric field (BIEF) *via* interfacial electronic redistribution between the two components. As shown in Fig. 3(d), DFT calculations reveal that the desolvation energy barrier for  $[\text{Zn}(\text{H}_2\text{O})_5]^{2+}$  complexes is significantly reduced at the  $\text{TiS}_2$ - $\text{TiO}_2$  interface (2.97 eV) compared to pure  $\text{TiS}_2$  (3.42 eV), highlighting the desolvation-facilitating role of the heterojunction.

To experimentally validate this effect, the authors compared a  $\text{TiS}_2$ - $\text{TiO}_2$  electrode (TSO-2, prepared *via* 2 min  $\text{O}_2$  plasma treatment) and a pure  $\text{TiS}_2$  electrode (TS) using electrochemical quartz crystal microbalance (EQCM). As shown in Fig. 3(e) and (f), the TSO-2 electrode exhibits a mass change per electron ( $\sim 27.4 \text{ g mol}^{-1}$ ) close to the theoretical value for bare  $\text{Zn}^{2+}$  insertion, indicating effective desolvation at the interface. In contrast, the TS electrode shows a higher mass change ( $\sim 39.6 \text{ g mol}^{-1}$ ), consistent with hydrated  $\text{Zn}^{2+}$  ( $[\text{Zn}(\text{H}_2\text{O})]^{2+}$ ) co-intercalation. These findings confirm that the built-in electric field at the  $\text{TiS}_2$ - $\text{TiO}_2$  interface promotes  $\text{Zn}^{2+}$  desolvation and alters the nature of the intercalating species. Altogether, this heterostructure design mitigates strain from hydrated ion insertion, promotes fast  $\text{Zn}^{2+}$  transport, and enables high-rate cycling (*e.g.*,  $160.9 \text{ mAh g}^{-1}$  at  $5 \text{ A g}^{-1}$ ).

Complementary work by Sun *et al.* employed  $\text{Ca}^{2+}$  pre-intercalation in  $\text{V}_2\text{O}_5$  to widen the interlayer spacing, which facilitates partial desolvation of  $\text{Zn}^{2+}$  upon insertion and enhances both capacity and cycling stability.<sup>45</sup> These lattice-level adjustments further highlight the role of interfacial field effects in regulating desolvation kinetics.

**3.1.3 Artificial cathode–electrolyte interphase confinement.** Beyond promoting desolvation, artificial cathode–electrolyte interphase (CEI) can also suppress active material dissolution and unwanted side reactions at the cathode surface. By confining  $\text{Zn}^{2+}$  desolvation within a well-structured interface, such designs improve long-term cycling stability.

Dai *et al.* designed a  $\text{Zn}_x(\text{OTf})_y(\text{OH})_{2x-y}n\text{H}_2\text{O}$  ( $\text{ZnOTf-LDH}$ ) interphase that functions as a selective ion-conducting layer on vanadium oxide cathodes.<sup>44</sup> As shown in Fig. 3(g), molecular dynamics simulations reveal that  $\text{Zn}^{2+}$  exhibits much higher diffusivity than  $\text{VO}_2^+$  or  $\text{VO}^{2+}$  across the  $\text{ZnOTf-LDH}$  layer, as confirmed by their distinct mean square displacements and diffusion coefficients. This selectivity stems from stronger electrostatic interactions between  $\text{ZnOTf-LDH}$  and vanadium species, which limit their mobility. Meanwhile,  $\text{Zn}^{2+}$  is efficiently transported and partially desolvated at the interface. Fig. 3(h) shows that  $\text{Zn}^{2+}$  exhibits stronger adsorption to the  $\text{ZnOTf-LDH}$  surface compared to  $\text{H}_2\text{O}$ , reflecting the interphase's combined zincophilic and hydrophobic character. This facilitates  $\text{Zn}^{2+}$  capture while excluding water molecules and promoting the desolvation of hydrated  $\text{Zn}^{2+}$ , as evidenced by

electrochemical impedance spectroscopy (EIS) measurements at different temperatures and supporting simulations, which revealed reduced charge-transfer resistance and lower activation energy for interfacial  $\text{Zn}^{2+}$  transport. Cyclic voltammetry (CV) measurements further confirm that the  $\text{ZnOTf-LDH}$  layer stabilizes interfacial ion flux, suppresses vanadium dissolution, and maintains redox activity during cycling (Fig. 3(i)). As a result, the cathode retains capacity over extended operation. This interphase exemplifies how structural confinement and selective ion affinity can enhance both  $\text{Zn}^{2+}$  kinetics and interfacial stability.

Zheng *et al.*<sup>46</sup> applied polydopamine (PDA) coatings to  $\text{NH}_4\text{V}_4\text{O}_{10}$  to create zincophilic layers that attract  $\text{Zn}^{2+}$ , lower desolvation barriers, and inhibit parasitic reactions. In a related system, Jiang *et al.*<sup>47</sup> reported PEDOT-modified  $\text{V}_5\text{O}_{12} \cdot 6\text{H}_2\text{O}$  cathodes that integrate hydrophobic and zincophilic properties, enabling balanced  $\text{Zn}^{2+}$  interfacial behavior and robust cycling under various conditions.

These studies illustrate that regulating  $\text{Zn}^{2+}$  desolvation at the cathode–electrolyte interface, whether through water masking, electric field effects, or artificial interphases, offers a coherent strategy to enhance  $\text{Zn}^{2+}$  transport kinetics, suppress material degradation, and extend the operational lifetime of AZIBs.

## 3.2 Anode–electrolyte interfacial desolvation

Efficient  $\text{Zn}^{2+}$  desolvation at the anode interface is essential for stabilizing Zn plating and suppressing side reactions like hydrogen evolution. Although numerous strategies have been proposed for modifying Zn metal anodes, we briefly summarize three representative interfacial approaches, including catalytic regulation, electronic tuning, and solvation structure modulation. The main emphasis of this review, however, lies slightly more on cathode-side interfacial processes.

**3.2.1 Atomic catalytic desolvation.** Atomic-level catalysts can effectively weaken  $\text{Zn}^{2+}$ - $\text{H}_2\text{O}$  coordination and reduce desolvation barriers. Zhang *et al.* anchored single Fe atoms onto  $\text{Ti}_3\text{C}_2\text{T}_x$  MXene, forming  $\text{SAFe@MXene}$  interfaces that redistributed local electron density and disrupted hydration shells.<sup>48</sup> DFT calculations revealed that interfacial charge redistribution induced by atomic Fe significantly lowered the energy barrier for stepwise  $\text{Zn}^{2+}$  dehydration (Fig. 4(a)). Specifically, the desolvation energy for  $[\text{Zn}(\text{H}_2\text{O})_6]^{2+}$  progressively decreased with each water molecule removed, and this energy barrier was consistently lower at the  $\text{SAFe@MXene}$  interface compared to pristine Zn. In addition, adsorption energy calculations (Fig. 4(b)) revealed that Zn atoms exhibit stronger binding to the  $\text{SAFe@MXene}$  surface ( $-1.26 \text{ eV}$ ) compared to MXene ( $-0.88 \text{ eV}$ ) and pristine Zn ( $-0.11 \text{ eV}$ ), confirming the enhanced  $\text{Zn}^{2+}$  affinity at the engineered interface. These theoretical insights support the observed electrochemical improvements, including enhanced Zn plating reversibility and effective suppression of dendrite growth under harsh cycling conditions. Related catalytic designs have also been proposed using crown ether additives,<sup>49</sup> pore-sieving structures,<sup>50</sup> and  $\text{CeO}_{2-x}$  catalytically active suspension electrolytes.<sup>51</sup>





**Fig. 4** Representative anode–electrolyte interfacial desolvation regulation strategies in AZIBs. (a) DFT-calculated desolvation energy profile for stepwise Zn<sup>2+</sup> dehydration on pristine Zn and SAFe@MXene-Zn surfaces (SA denotes single-atom). (b) Zn<sup>2+</sup> adsorption energies on pristine Zn, MXene-Zn, and SAFe@MXene-Zn surfaces, indicating enhanced Zn<sup>2+</sup> affinity at the catalytic interface. Reproduced from ref. 48 Copyright (2025), with permission from American Chemical Society. (c) DFT-calculated adsorption energies of Zn(H<sub>2</sub>O)<sub>6</sub><sup>2+</sup> cluster on pure carbon and various nitrogen-doped carbon surfaces. (d) Dissociation energy of Zn(H<sub>2</sub>O)<sub>6</sub><sup>2+</sup> cluster in various chemical environments. Reproduced from ref. 52 under the Creative Commons CC BY license. (e) Experimental pair distribution function (PDF)  $G(r)$  (top) and simulated radial distribution function (RDF)  $g(r)$  (bottom) of 1 and 4 M ZnSO<sub>4</sub> electrolytes. (f) Deconvolution of the stretching vibration of H<sub>2</sub>O. The pie chart shows the proportions of the local weak hydrogen-bond/W-H (high wavenumber) and strong hydrogen-bond/S-H (low wavenumber). DDAA refers to a double donor–double acceptor configuration, DDA to a double donor–single acceptor, DAA to a single donor–double acceptor, and DA to a single donor–single acceptor. (g) *In situ* FTIR spectra were collected during the Zn-electroplating/stripping with the variation of spectra color from blue (Zn-plating, bottom) to orange (Zn-stripping, top). (h) Evolution of the relative absorbance  $A(t_n) - A(t_0)$  of 1 M ZnSO<sub>4</sub> during Zn-plating (bottom) and Zn stripping (top). Reproduced from ref. 55 Copyright (2024), with permission from American Chemical Society.

**3.2.2 Electronic structure-mediated desolvation.** Modulating interfacial electronic structures offers a powerful approach to accelerate Zn<sup>2+</sup> desolvation by altering local charge distributions and tuning the Fermi level. Guo *et al.*<sup>52</sup> designed nitrogen-doped carbon (NC) coatings on Nafion substrates to reshape the interfacial potential landscape between Zn metal and the electrolyte. The NC layer introduced abundant non-coordinating nitrogen sites that redistributed interfacial charges and shifted the Fermi level upward, thereby destabilizing the Zn<sup>2+</sup> hydration shell. As shown in Fig. 4(c), DFT

calculations indicated stronger Zn(H<sub>2</sub>O)<sub>6</sub><sup>2+</sup> adsorption on NC, especially at pyridinic and graphitic nitrogen sites. Furthermore, the dissociation energy of Zn(H<sub>2</sub>O)<sub>6</sub><sup>2+</sup> was markedly reduced in these nitrogen-rich environments (Fig. 4(d)), demonstrating that electronic redistribution at the interface plays a critical role in facilitating Zn<sup>2+</sup> dehydration. Collectively, these effects boosted Zn<sup>2+</sup> desolvation kinetics, achieving highly reversible Zn plating and mitigating dendrite formation.

Additional strategies for electronic-structure modulation include the use of molecular cage additives that offer multi-



site  $\text{Zn}^{2+}$  coordination,<sup>53</sup> and sulfonic acid-functionalized frameworks that locally tune charge density at the interface.<sup>54</sup>

**3.2.3 Dynamic solvation reconstruction.** Revealing the dynamic nature of  $\text{Zn}^{2+}$  solvation structures under electrochemical cycling has inspired new strategies to regulate interfacial behavior. Yu *et al.*<sup>55</sup> uncovered that increasing  $\text{ZnSO}_4$  concentration from 1 M to 4 M compresses the solvation shell and strengthens Zn–O interactions, as shown by molecular dynamics (MD) simulations and pair distribution function analysis (Fig. 4(e)). Time-resolved Fourier transform infrared (FTIR) spectra further revealed a progressive increase in the fraction of strong hydrogen bonds (O–H stretch at lower wavenumbers) and gradual, reversible vibrational shifts during plating/stripping (Fig. 4(f) and (g)), indicating  $\text{Zn}^{2+}$  dehydration during plating and re-solvation upon stripping. These results demonstrate that  $\text{Zn}^{2+}$  solvation is not static but dynamically reconstructs in response to the electrochemical environment (Fig. 4(h)). Aligning with this mechanistic insight, several interfacial engineering strategies have been developed to leverage dynamic solvation behavior. For example, Lu *et al.*<sup>56</sup> introduced self-assembled bio-interfacial bilayers to modulate local hydrogen-bonding networks, while Dong *et al.*<sup>51</sup> designed catalytically adaptive suspension electrolytes to promote *in situ*  $\text{Zn}^{2+}$  dehydration. These strategies leverage dynamic solvation reconstruction as a regulatory handle, enabling

adaptive control of  $\text{Zn}^{2+}$  flux, improve reversibility, and effective dendrite suppression.

## 4. Interfacial storage of species from water dissociation

### 4.1 $\text{H}^+$ storage regulation

The high hydration enthalpy of  $\text{Zn}^{2+}$ , reaching  $2046 \text{ kJ mol}^{-1}$ , not only results in significant desolvation barriers but also facilitates partial water dissociation at the electrode–electrolyte interface.<sup>57</sup> This interfacial hydrolysis process continuously generates additional  $\text{H}^+$  and  $\text{OH}^-$  species, which potentially participate in charge storage reactions across multiple systems, often contributing substantial capacity beyond traditional  $\text{Zn}^{2+}$  intercalation.

**4.1.1  $\text{Zn}^{2+}/\text{H}^+$  co-storage.** In many  $\text{Zn}^{2+}$  intercalation hosts, hydrated  $\text{Zn}^{2+}$  ions and protons can simultaneously participate in the storage process, giving rise to  $\text{Zn}^{2+}/\text{H}^+$  co-intercalation behavior. A representative example<sup>58</sup> is found in S-doped  $\text{MoO}_2$ . As illustrated in Fig. 5(a), the CV curve exhibits two distinct cathodic peaks, which correspond to the successive insertion of  $\text{H}^+$  and  $\text{Zn}^{2+}$  into the electrode. Simultaneously, the *in situ* EQCM reveals a two-step mass change during discharge, as shown in Fig. 5(b). The first mass increase from point B to C corresponds to  $\text{H}^+$  insertion, with a mass-to-charge ratio ( $m/z$ )



**Fig. 5** Representative mechanisms of proton storage regulation in AZIBs. (a) CV curves of the aqueous Zn||S-MoO<sub>2</sub> at  $1.5 \text{ mV s}^{-1}$  and the simultaneous response of the mass change of S-MoO<sub>2</sub> electrode as recorded by EQCM. ZHS denotes basic zinc sulfate. (b) Mass weight versus charge curve during the discharging and charging process. Reproduced from ref. 58 Copyright (2023), with permission from Wiley-VCH. (c) CV curves of the Zn||2M ZnSO<sub>4</sub> + 0.5 M MnSO<sub>4</sub>||ZnO cell at  $0.2 \text{ mV s}^{-1}$ , from 0.8 to 1.8 V vs. Zn/Zn<sup>2+</sup>. Reproduced from ref. 63 Copyright (2022), with permission from Wiley-VCH. (d) Quasi-elastic neutron scattering (QENS) analysis of various hybrid aqueous-non aqueous (HANE) systems. (e) Typical voltage profile of VPO<sub>4</sub>F between 0.2 and 2.1 V in the 4 m Zn(OTf)<sub>2</sub>·H<sub>2</sub>O electrolyte. Inset: H/Zn atom ratio in the discharged VPO<sub>4</sub>F electrode. (f) Typical voltage profile of Zn<sub>x</sub>H<sub>y</sub>VPO<sub>4</sub> between 0.2 and 2.1 V in 2 m Zn(OTf)<sub>2</sub>·2H<sub>2</sub>O–propylene carbonate (PC) electrolyte. Reproduced from ref. 69 Copyright (2021), with permission from Wiley-VCH.



of 18.9 g mol<sup>-1</sup>, matching the molar mass of H<sub>3</sub>O<sup>+</sup>. The subsequent sharper mass increase from point C to D yields an *m/z* of 69.8 g mol<sup>-1</sup>, indicative of Zn<sup>2+</sup> insertion coupled with formation of hydrated byproducts. During charging, the mass decrease proceeds in reverse order, with Zn<sup>2+</sup> and H<sup>+</sup> sequentially extracted (*m/z* = 65.6 and 18.9 g mol<sup>-1</sup>, respectively), confirming their co-contribution to the overall capacity.

Similar Zn<sup>2+</sup>/H<sup>+</sup> co-insertion behavior has been widely observed in hydrated vanadium oxides such as V<sub>2</sub>O<sub>5</sub>·*n*H<sub>2</sub>O and VO<sub>2</sub>. In these systems, the presence of pre-intercalated water layers provides expanded interlayer spacing and abundant hydrogen bonding sites, which effectively stabilize the co-inserted Zn<sup>2+</sup> and H<sup>+</sup> ions. For example, in V<sub>2</sub>O<sub>5</sub>·*n*H<sub>2</sub>O, quantitative analyses suggest that H<sup>+</sup> contributes nearly 44% of the total capacity due to its faster insertion kinetics and smaller ionic size.<sup>59</sup> In VO<sub>2</sub>, Li *et al.* demonstrated proton insertion with Zn<sup>2+</sup> being mostly involved in surface byproduct formation.<sup>60</sup>

A unique H<sup>+</sup> “lubrication” effect has also been proposed in MoS<sub>2</sub>-based hosts by Li *et al.*, where pre-inserted protons significantly lower the migration barrier for subsequent Zn<sup>2+</sup> intercalation. Theoretical calculations reveal that the Zn<sup>2+</sup> insertion energy barrier can be reduced from 0.97 eV to 0.41 eV upon prior H<sup>+</sup> insertion, thus enhancing Zn<sup>2+</sup> diffusion kinetics and reversibility.<sup>61</sup>

**4.1.2 H<sup>+</sup>-dominated intercalation.** In certain systems, H<sup>+</sup> serves as the exclusive or dominant charge carrier for intercalation, a behavior particularly prevalent in MnO<sub>2</sub>-based cathodes. Using α-MnO<sub>2</sub> as a model system, Yuan *et al.* systematically revealed that Zn<sup>2+</sup> insertion is energetically unfavorable, while H<sup>+</sup> insertion into the 1 × 1 and 2 × 2 tunnels dominates the storage mechanism.<sup>62</sup> The insertion of H<sup>+</sup> induces slight lattice expansion and Mn–OH bond formation while preserving structural reversibility. Chen *et al.*<sup>63</sup> further revealed that the H<sup>+</sup>-dominated intercalation mechanism does not require MnO<sub>2</sub> as the initial cathode material. Instead, as long as the electrode surface permits H<sup>+</sup> uptake (*e.g.*, Zn||2 M ZnSO<sub>4</sub> + 0.5 M MnSO<sub>4</sub>||ZnO cell as shown in Fig. 5(c)), proton insertion triggers local OH<sup>-</sup> enrichment and subsequent formation of Zn<sub>4</sub>SO<sub>4</sub>·(OH)<sub>6</sub>·*x*H<sub>2</sub>O (ZHS). This ZHS layer then reacts with Mn<sup>2+</sup> in the electrolyte to generate electrochemically active Zn<sub>*x*</sub>MnO(OH)<sub>2</sub>, which supports reversible H<sup>+</sup> intercalation analogous to that in conventional MnO<sub>2</sub>-based systems. Earlier, Liu *et al.*<sup>64</sup> had also demonstrated that MnO<sub>2</sub> undergoes a proton-coupled conversion reaction to form MnOOH intermediates, with minimal Zn<sup>2+</sup> participation.

Beyond MnO<sub>2</sub>, proton-dominant behavior extends to other hosts. For instance, recent studies on Na<sub>0.12</sub>Zn<sub>0.25</sub>V<sub>2</sub>O<sub>5</sub>·2.5H<sub>2</sub>O layered structures highlight highly dynamic proton conduction pathways in V<sub>2</sub>O<sub>5</sub>-based hosts, wherein H<sup>+</sup> migration proceeds *via* Zundel pair-dancing mechanisms, enabling ultrafast pseudocapacitive response even at extremely high current densities, effectively excluding Zn<sup>2+</sup> intercalation at ultrahigh rates.<sup>65</sup> In parallel, in TiS<sub>2</sub>, facet engineering enabled H<sup>+</sup>-dominated storage with suppressed hydrogen evolution under (011) orientation.<sup>66</sup> Furthermore, pH and electrolyte volume have been shown to directly influence H<sup>+</sup> participation. Using V<sub>2</sub>O<sub>5</sub>

electrodes, Lee *et al.*<sup>67</sup> demonstrated that smaller electrolyte volumes or higher pH significantly suppress H<sup>+</sup> insertion, whereas lower pH and larger electrolyte reservoirs facilitate greater H<sup>+</sup> contribution.

Moreover, co-doping strategies have emerged as a powerful approach to further enhance H<sup>+</sup> insertion behavior. Chen *et al.*<sup>68</sup> showed that Co<sup>2+</sup> pre-insertion into MnO<sub>2</sub> tunnels stabilizes the lattice, allowing more favorable H<sup>+</sup> intercalation while excluding Zn<sup>2+</sup> insertion. DFT calculations revealed significantly lower migration barriers for H<sup>+</sup> compared to Zn<sup>2+</sup> within the Co-stabilized tunnel structures, underscoring the proton-dominant storage mechanism.

**4.1.3 H<sup>+</sup> intercalation suppression.** While H<sup>+</sup> insertion can enhance capacity, its excessive participation may also induce structural instability and parasitic reactions such as Mn dissolution and basic zinc salt precipitation. To address this, strategies have been developed to suppress H<sup>+</sup> intercalation while preserving Zn<sup>2+</sup> storage reversibility. Zhang *et al.*<sup>69</sup> demonstrated that VPO<sub>4</sub>F frameworks, owing to their strong electronegativity and limited hydrogen-bonding sites, effectively exclude H<sup>+</sup> and favor Zn<sup>2+</sup>-dominated storage. This selective behavior is supported by quasi-elastic neutron scattering (QENS) in Fig. 5(d), where reduced water mobility under concentrated Zn(OTf)<sub>2</sub> electrolytes reflects suppressed proton dynamics. Fig. 5(e) shows that Zn<sub>*x*</sub>H<sub>*y*</sub>VPO<sub>4</sub>F delivers a capacity corresponding to ~0.14 Zn<sup>2+</sup> and ~0.6 H<sup>+</sup> per formula unit, indicating a dominant Zn<sup>2+</sup> contribution despite residual proton uptake. Notably, Fig. 5(f) reveals stable voltage profiles over multiple cycles in a hybrid Zn(OTf)<sub>2</sub>·2H<sub>2</sub>O–propylene carbonate (PC) electrolyte, with capacities (~90 mAh g<sup>-1</sup>) primarily derived from Zn<sup>2+</sup> insertion. These results collectively highlight the potential of tailored frameworks like VPO<sub>4</sub>F in enabling Zn<sup>2+</sup>-dominant intercalation with suppressed proton-induced side reactions, paving the way for more stable and efficient aqueous Zn-ion batteries.

It is worth noting that despite widespread discussion of “H<sup>+</sup> insertion,” the actual origin of these protons is rarely examined in detail. At the coin cell level, quantitative analysis reveals that substantial proton involvement cannot plausibly arise from pre-existing free H<sup>+</sup> ions in the bulk electrolyte alone. For example, in a Zn||VO<sub>2</sub> cell using a typical lab-level cathode mass of 1–5 mg and 80–200 μL of 2 M ZnSO<sub>4</sub> or 3 M Zn(OTf)<sub>2</sub> electrolyte (pH ≈ 4),<sup>60,70–74</sup> the total amount of H<sup>+</sup> in the bulk electrolyte is only 8–20 nmol. In contrast, experimental capacities of 250–400 mAh g<sup>-1</sup> require 4–37 μmol of proton charge storage, which exceeds the available H<sup>+</sup> supply by more than two to three orders of magnitude. This discrepancy clearly indicates that continuous interfacial water dissociation must occur to generate additional protons during cycling. As elaborated in the following section, similar interfacial dissociation processes also underpin hydroxide-based charge storage mechanisms.

## 4.2 OH<sup>-</sup> storage through water dissociation

Compared with the extensively studied Zn<sup>2+</sup> and H<sup>+</sup> storage paradigms, OH<sup>-</sup>-based charge storage remains relatively



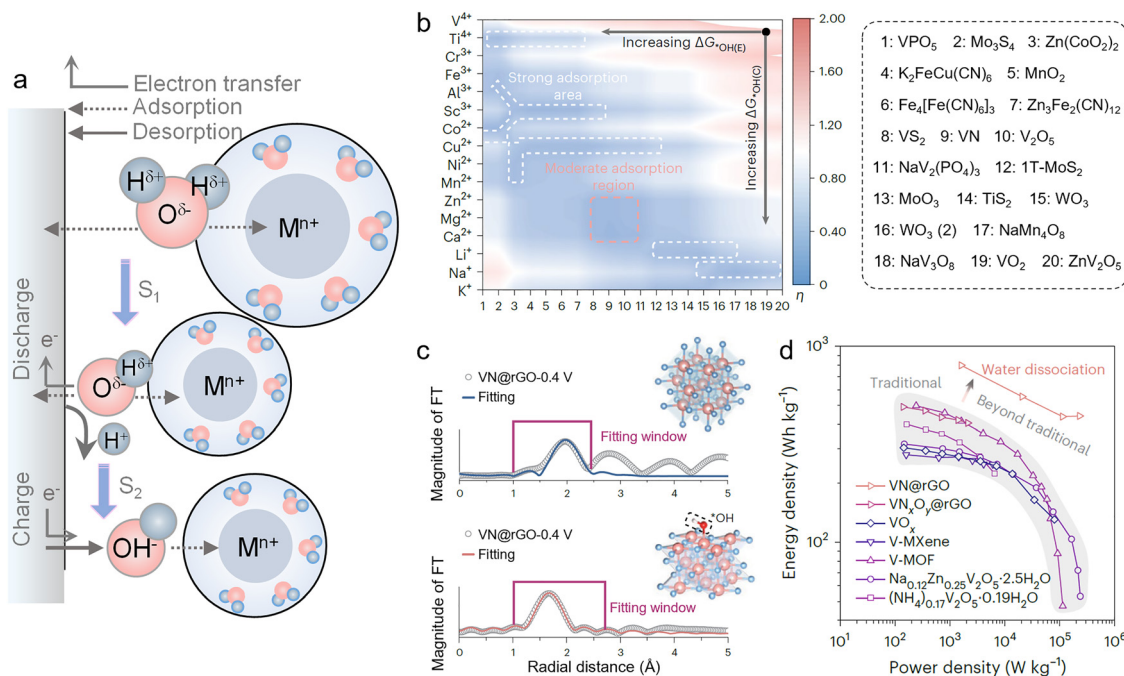


Fig. 6 Zn<sup>2+</sup>-mediated interfacial OH<sup>-</sup> storage in VN cathodes. (a) Schematic showing Zn<sup>2+</sup> polarization-induced water dissociation and reversible OH<sup>-</sup> adsorption at the electrode surface. (b) Contour plot of water dissociation activity as a function of \*OH adsorption energy, comparing different metal ions and cathode materials. (c) Operando extended X-ray absorption fine structure (EXAFS) fitting results indicating surface-confined \*OH adsorption on VN@rGO during discharge, with no lattice expansion. (d) Comparison of rate performance between water dissociation rendered OH<sup>-</sup> storage and conventional Zn<sup>2+</sup> intercalation. Reproduced from ref. 77 Copyright (2024), with permission from Springer Nature.

underexplored and mechanistically distinct, especially in mildly acidic aqueous zinc-ion battery systems. While Zn<sup>2+</sup> and H<sup>+</sup> typically undergo intercalation, OH<sup>-</sup> participates in surface-mediated redox reactions that proceed *via* confined interfacial charge transfer rather than bulk ion diffusion. This gives rise to pseudocapacitive behavior that is fundamentally different from conventional intercalation mechanisms. Recent studies have further demonstrated that OH<sup>-</sup>, generated through interfacial water dissociation, can serve as efficient and reversible charge carriers under such conditions.

Initial evidence for OH<sup>-</sup> involvement emerged from systems where Zn<sup>2+</sup> hydrolysis leads to the formation of solid hydroxide phases such as basic zinc sulfate (ZHS), which is particularly intriguing under mildly acidic electrolytes because the generation of seemingly alkaline compounds is not straightforward. These observations indicated that Zn<sup>2+</sup> could polarize adjacent water molecules, triggering water dissociation and local accumulation of OH<sup>-</sup>. This process not only produces H<sup>+</sup> that may participate in intercalation mentioned above but simultaneously generates OH<sup>-</sup> species that contribute to charge storage by being captured or fixed as solid byproducts.<sup>75,76</sup>

Moving beyond these indirect pathways, Dai *et al.*<sup>77</sup> recently established a catalytic model in which Zn<sup>2+</sup> ions polarize adjacent water molecules, thereby facilitating continuous water dissociation at the electrode–electrolyte interface, as shown in Fig. 6(a). In this model, the OH<sup>-</sup> species generated reversibly adsorbed at the electrode surface, with their storage kinetics primarily governed by the binding strength of \*OH to the

electrode surface. Through systematic screening of various combinations of cations and cathode materials, vanadium nitride (VN) was identified as the optimal candidate, featuring the most balanced Zn<sup>2+</sup>–H<sub>2</sub>O and VN–H<sub>2</sub>O interactions, showing a moderate \*OH binding energy that ensures fast kinetics while minimizing side reactions, as illustrated in Fig. 6(b).

This mechanism was experimentally validated through operando (real-time and *in situ*) extended X-ray absorption fine structure (EXAFS) measurements, which confirmed that OH<sup>-</sup> adsorption occurs without any detectable lattice distortion in the VN@rGO electrode. This observation supports the conclusion that charge storage takes place predominantly at the surface rather than within the bulk lattice, as depicted in Fig. 6(c). In addition, electrochemical testing revealed that VN@rGO achieves a high specific capacity of 577.1 mAh g<sup>-1</sup> even at an ultrahigh current density of 300 A g<sup>-1</sup>, significantly outperforming Zn<sup>2+</sup>-dominated systems under comparable conditions, as shown in Fig. 6(d).

These results suggest a fundamental shift in the design principles for AZIBs. Instead of relying solely on traditional ion migration through the solid phase, this approach emphasizes interfacial catalysis as the primary mechanism governing charge storage. Careful tuning of interfacial chemistry to optimize \*OH adsorption enables water dissociation products, previously considered undesirable, to serve as highly effective and kinetically favorable charge carriers. It is also important to note that OH<sup>-</sup> storage mechanisms are typically sensitive to





Fig. 7 Roadmap for promising interfacial design trends in AZIBs (next 5–10 years).

local pH fluctuations, which may trigger side reactions such as precipitation or phase instability over extended cycling.

## 5. Summary and outlook

Interfacial regulation has emerged as a powerful strategy to address the fundamental transport and stability challenges in AZIBs. This review systematically summarizes recent progresses in both solid–solid and solid–liquid interfaces, highlighting diverse yet complementary approaches for facilitating  $\text{Zn}^{2+}$  migration, desolvation, and interfacial charge transfer. At solid–solid interfaces, strategies leveraging internal electrostatic fields, interfacial chemical bonding, and electron–ion decoupling significantly reduce  $\text{Zn}^{2+}$  diffusion barriers while enhancing structural stability and reaction reversibility. For solid–liquid interfaces, engineered desolvation layers, catalytic desolvation sites, and dynamic solvation reconstruction have been successfully demonstrated to promote rapid  $\text{Zn}^{2+}$  desolvation and suppress parasitic side reactions.

Beyond classical  $\text{Zn}^{2+}$  intercalation mechanisms, recent studies have identified that products derived from interfacial water dissociation, specifically  $\text{H}^+$  and  $\text{OH}^-$ , offer alternative and highly efficient charge storage pathways. The interfacial water dissociation mediated by  $\text{Zn}^{2+}$  polarization provides a continuous supply of  $\text{H}^+$  and  $\text{OH}^-$ , enabling mechanisms such as  $\text{H}^+$ -dominated intercalation and surface-confined  $\text{OH}^-$  pseudocapacitance. These emerging pathways enhance battery capacity and rate capability, while redefining the role of interfacial reactions in overall performance.

Looking forward, further progress will rely on deepening mechanistic understanding of interfacial chemical dynamics under realistic operating conditions such as high mass loadings and a balanced negative-to-positive (N/P) capacity ratio. In practice, achieving a rational N/P ratio critically depends on preparing high-mass-loading cathodes, yet maintaining electrochemical performance under such conditions remains a major challenge in AZIBs.<sup>78</sup> Rational interfacial design is therefore expected to play a pivotal role in mitigating transport limitations and enabling stable operation at high areal capacities. To fully unravel these interfacial functions under practically relevant conditions, advanced operando characterization, multi-scale simulations, and interface-specific probes are essential to resolve the intricate interplay among  $\text{Zn}^{2+}$  transport, water dissociation dynamics, and interfacial phase evolution. Moreover, deliberate design of catalytic interfaces that precisely regulate water dissociation and capture its dissociation products offers promising opportunities to break conventional

trade-offs between capacity, rate capability, and long-term stability.

While many of the interfacial strategies discussed in this review show strong potential, most remain at the laboratory or proof-of-concept stage. Further studies on scalability, compatibility, and long-term stability will be essential to assess their commercial relevance and guide the transition toward practical applications.

If successfully translated into practical systems, interfacial regulation holds great promise to enable unprecedented levels of fast charging, long cycling life, and real-world viability for large-scale energy storage using AZIBs. A conceptual roadmap outlining promising interfacial design trends over the next 5–10 years is presented in Fig. 7 to guide future research priorities. Furthermore, the insights and strategies reviewed herein are expected to provide valuable guidance for advancing not only other multivalent-ion battery systems (where ion size, solvation structures, and interfacial phenomena similarly dictate performance) but also conversion-type chemistries such as Zn–S and Zn– $\text{I}_2$  batteries, in which interfacial storage processes play an increasingly dominant role.

## Conflicts of interest

There are no conflicts to declare.

## Data availability

No primary research results, software or code have been included and no new data were generated or analysed as part of this review.

## Acknowledgements

This work was also supported by the EPSRC (EP/V027433/3, EP/L015862/1), UK Research and Innovation (UKRI) under the UK government's Horizon Europe funding guarantee (101077226; EP/Y008707/1).

## References

- 1 X. Jia, C. Liu, Z. G. Neale, J. Yang and G. Cao, *Chem. Rev.*, 2020, **120**, 7795–7866.
- 2 C. Xu, B. Li, H. Du and F. Kang, *Angew. Chem., Int. Ed.*, 2012, **51**, 933–935.
- 3 D. Kundu, B. D. Adams, V. Duffort, S. H. Vajargah and L. F. Nazar, *Nat. Energy*, 2016, **1**, 16119.



- 4 H. Pan, Y. Shao, P. Yan, Y. Cheng, K. S. Han, Z. Nie, C. Wang, J. Yang, X. Li, P. Bhattacharya, K. T. Mueller and J. Liu, *Nat. Energy*, 2016, **1**, 16039.
- 5 W. Zong, J. Li, C. Zhang, Y. Dai, Y. Ouyang, L. Zhang, J. Li, W. Zhang, R. Chen, H. Dong, X. Gao, J. Zhu, I. P. Parkin, P. R. Shearing, F. Lai, K. Amine, T. Liu and G. He, *J. Am. Chem. Soc.*, 2024, **146**, 21377–21388.
- 6 R. Chen, W. Zhang, C. Guan, Y. Zhou, I. Gilmore, H. Tang, Z. Zhang, H. Dong, Y. Dai, Z. Du, X. Gao, W. Zong, Y. Xu, P. Jiang, J. Liu, F. Zhao, J. Li, X. Wang and G. He, *Angew. Chem., Int. Ed.*, 2024, **63**, e202401987.
- 7 S. Mariyappan, T. Marchandier, F. Rabuel, A. Iadecola, G. Rousse, A. V. Morozov, A. M. Abakumov and J. M. Tarascon, *Chem. Mater.*, 2020, **32**, 1657–1666.
- 8 X. Zhang, S. Yang, X. Shan, S. Li and S. Tang, *Phys. Chem. Chem. Phys.*, 2019, **21**, 23697–23704.
- 9 H. Yao, H. Yu, Y. Zheng, N. W. Li, S. Li, D. Luan, X. W. D. Lou and L. Yu, *Angew. Chem., Int. Ed.*, 2023, **62**, e202315257.
- 10 F. Wan, Y. Zhang, L. Zhang, D. Liu, C. Wang, L. Song, Z. Niu and J. Chen, *Angew. Chem., Int. Ed.*, 2019, **58**, 7062–7067.
- 11 L. Wang, S. Yan, C. D. Quilty, J. Kuang, M. R. Dunkin, S. N. Ehrlich, L. Ma, K. J. Takeuchi, E. S. Takeuchi and A. C. Marschilok, *Adv. Mater. Interfaces*, 2021, **8**, 2002080.
- 12 R. W. Chen, C. Y. Zhang, J. W. Li, Z. J. Du, F. Guo, W. Zhang, Y. H. Dai, W. Zong, X. Gao, J. X. Zhu, Y. Zhao, X. H. Wang and G. J. He, *Energy Environ. Sci.*, 2023, **16**, 2540–2549.
- 13 X. M. Li, X. Y. Wang, L. T. Ma and W. Huang, *Adv. Energy Mater.*, 2022, **12**, 2202068.
- 14 S. Chen, D. Ji, Q. Chen, J. Ma, S. Hou and J. Zhang, *Nat. Commun.*, 2023, **14**, 3526.
- 15 L. Cao, D. Li, T. Pollard, T. Deng, B. Zhang, C. Yang, L. Chen, J. Vatamanu, E. Hu, M. J. Hourwitz, L. Ma, M. Ding, Q. Li, S. Hou, K. Gaskell, J. T. Fourkas, X. Q. Yang, K. Xu, O. Borodin and C. Wang, *Nat. Nanotechnol.*, 2021, **16**, 902–910.
- 16 C. Liu, Q. Li, Y. Lin, Z. Wei, Y. Yang, C. Han, M. Zhu, H. Zhang and H. Li, *Nano Res. Energy*, 2023, **2**, e9120064.
- 17 Q. Zhang, J. Luan, X. Huang, Q. Wang, D. Sun, Y. Tang, X. Ji and H. Wang, *Nat. Commun.*, 2020, **11**, 3961.
- 18 Y. X. Zhang, Y. Z. Y. Chen, Y. Jiang, J. Wang, X. Y. Zheng, B. Han, K. S. Xia, Q. Gao, Z. Cai, C. G. Zhou and R. M. Sun, *Adv. Funct. Mater.*, 2023, **33**, 2212785.
- 19 D. Li, L. Cao, T. Deng, S. Liu and C. Wang, *Angew. Chem., Int. Ed.*, 2021, **60**, 13035–13041.
- 20 W. Zhang, Y. Dai, R. Chen, Z. Xu, J. Li, W. Zong, H. Li, Z. Li, Z. Zhang, J. Zhu, F. Guo, X. Gao, Z. Du, J. Chen, T. Wang, G. He and I. P. Parkin, *Angew. Chem., Int. Ed.*, 2023, **62**, e202212695.
- 21 W. Du, E. H. Ang, Y. Yang, Y. Zhang, M. Ye and C. C. Li, *Energy Environ. Sci.*, 2020, **13**, 3330–3360.
- 22 J. Shin, J. Lee, Y. Park and J. W. Choi, *Chem. Sci.*, 2020, **11**, 2028–2044.
- 23 W. Zhang and G. He, *Angew. Chem., Int. Ed.*, 2023, **62**, e202218466.
- 24 X. Zhang, L. Zhang, X. Jia, W. Song and Y. Liu, *Nano-Micro Lett.*, 2024, **16**, 75.
- 25 T. Wang, S. Tang, Y. Xiao, W. Xiang and J. S. Yu, *Energy Environ. Sci.*, 2025, **18**, 545–578.
- 26 X. Wang, B. Liu, Z. Xu, Y. Zhou, Y. Yang, H. Pan and G. Wang, *Adv. Energy Mater.*, 2025, **15**, 2405253.
- 27 P. H. Liang, T. F. Xu, K. J. Zhu, Y. Rao, H. J. Zheng, M. Wu, J. T. Chen, J. S. Liu, K. Yan, J. Wang and R. F. Zhang, *Energy Storage Mater.*, 2022, **50**, 63–74.
- 28 P. Cai, K. L. Wang, X. He, Q. X. Li, Z. C. Zhang, M. J. Li, H. M. Li, M. Zhou, W. Wang and K. Jiang, *Energy Storage Mater.*, 2023, **60**, 102835.
- 29 Y. Wang, J. Song and W. Y. Wong, *Angew. Chem., Int. Ed.*, 2023, **62**, e202218343.
- 30 X. L. Guo, C. G. Li, X. Y. Wang, Z. H. Li, H. Zeng, P. Hou, M. G. Xie, Y. X. Li, Z. Shi and S. H. Feng, *Sci. China: Chem.*, 2023, **66**, 1406–1416.
- 31 H. A. Zhai, H. B. Liu, Y. F. Zhang, J. J. Wen, W. Y. Yang, H. T. Xu, X. T. Yan, W. C. Peng and J. P. Liu, *J. Mater. Sci. Technol.*, 2024, **188**, 183–190.
- 32 X. Liu, W. Ni, Y. Wang, Y. Liang, B. Wu, G. Xu, X. Wei and L. Yang, *Small*, 2022, **18**, e2105796.
- 33 B. Q. Xiao, J. Chen, C. F. Hu, L. S. Mou, W. J. Yang, W. H. He, Z. B. Lu, S. L. Peng and J. J. Huang, *Adv. Funct. Mater.*, 2023, **33**, 2211679.
- 34 G. Q. Yuan, X. Wei, Y. C. Su, T. Y. Zhou, J. L. Hu, Y. An, S. L. Zhou, W. Q. Zhao, J. Xia and Y. Y. Liu, *Small*, 2024, **20**, e2308851.
- 35 N. U. R. Lashari, A. Kumar, I. Ahmed, J. Zhao, A. Hussain, U. Ghani, G. Luo, G. Yasin, M. A. Mushtaq, D. Liu and X. Cai, *Small*, 2024, **20**, e2309029.
- 36 N. Jiang, Y. Zeng, Q. Yang, P. D. Lu, K. Q. Qu, L. H. Ye, X. J. Lu, Z. Q. Liu, X. X. Li, Y. C. Tang, J. C. Cao, S. M. Chen, C. Y. Zhi and J. S. Qiu, *Energy Environ. Sci.*, 2024, **17**, 8904–8914.
- 37 C.-C. Chen and J. Maier, *Nat. Energy*, 2018, **3**, 102–108.
- 38 Y. Dai, X. Liao, R. Yu, J. Li, J. Li, S. Tan, P. He, Q. An, Q. Wei, L. Chen, X. Hong, K. Zhao, Y. Ren, J. Wu, Y. Zhao and L. Mai, *Adv. Mater.*, 2021, **33**, e2100359.
- 39 D. X. Liu, W. J. Wang, S. M. Li, X. J. Shen, H. J. Xie and H. Xu, *Adv. Funct. Mater.*, 2024, **34**, 2402584.
- 40 W. Zhong, Z. Y. Shen, J. L. Mao, S. C. Zhang, H. Cheng, Y. Kim and Y. Y. Lu, *Energy Environ. Sci.*, 2024, **17**, 2059–2068.
- 41 Q. Gou, H. Luo, Y. Zheng, Q. Zhang, C. Li, J. Wang, O. Odunmbaku, J. Zheng, J. Xue, K. Sun and M. Li, *Small*, 2022, **18**, e2201732.
- 42 L. Y. Ding, L. Wang, J. C. Gao, T. R. Yan, H. T. Li, J. Mao, F. Song, S. Fedotov, L. Y. Chang, N. Li, Y. F. Su, T. F. Liu and L. Zhang, *Adv. Funct. Mater.*, 2023, **33**, 2301648.
- 43 M. L. Chen, M. Zhou, Q. Y. Wang, C. Xu, S. Wang, J. Ning, T. Q. Wang, K. L. Wang and K. Jiang, *Adv. Funct. Mater.*, 2025, **35**, 2414032.
- 44 Y. Dai, C. Zhang, J. Li, X. Gao, P. Hu, C. Ye, H. He, J. Zhu, W. Zhang, R. Chen, W. Zong, F. Guo, I. P. Parkin, D. J. L. Brett, P. R. Shearing, L. Mai and G. He, *Adv. Mater.*, 2024, **36**, e2310645.
- 45 Q. Sun, H. Cheng, C. Sun, Y. Liu, W. Nie, K. Zhao, X. Lu and J. Zhou, *ACS Appl. Mater. Interfaces*, 2021, **13**, 60035–60045.



- 46 X. Zheng, Y. Zheng, Y. Tao, X. Zheng, Z. Chen, X. Wang, M. Shang, J. Du, S. Wu, Y. Pang, F. Wang and Z. Shen, *J. Alloys Compd.*, 2025, **1010**, 178140.
- 47 X. D. Jiang, T. D. Wang, M. Z. Ji, D. Ji, S. Y. Deng, G. H. Gao, J. Shen and G. M. Wu, *Adv. Funct. Mater.*, 2025, **35**, 2420686.
- 48 J. Zhang, L. Pan, L. Jia, J. Dong, C. You, C. Han, N. Tian, X. Cheng, B. Tang, Q. Guan, Y. Zhang, B. Deng, L. Lei, M. Liu, H. Lin and J. Wang, *Nano Lett.*, 2025, **25**, 3756–3765.
- 49 A. H. Wu, S. J. Zhang, Q. H. Li, W. X. Xue, C. Y. Li, B. J. Xi, W. T. Mao, K. Y. Bao and S. L. Xiong, *Adv. Energy Mater.*, 2025, **15**, 2404450.
- 50 G. J. Yang, Q. Zhang, Z. L. Liu, J. Song, Z. Y. Yin, Y. X. Zhao, S. H. Jiang, J. Q. Han, X. Li, H. Q. Yang, S. J. He and Z. X. Pei, *Adv. Energy Mater.*, 2025, 2501358.
- 51 J. Dong, X. Cheng, H. Yang, H. Li, H. Liu, L. Jia, Y. Zhang, Q. Guan, J. Jia, F. Wu, J. Zhang, M. Liu, H. Lin and J. Wang, *Adv. Mater.*, 2025, **37**, e2501079.
- 52 X. Guo, Q. Peng, R. Yang, G. Cao, J. Wen, K. Shin, Y. Zheng, S. Tunmee, C. Zou, Y. Zheng, X. Zhou and Y. Tang, *Natl. Sci. Rev.*, 2025, **12**, nwaf070.
- 53 J. Yan, H. Dou, M. Su, M. Xu, S. Liu, S. Qin, B. Zhang, K. Zong, L. Tan, X. Wang and Z. Chen, *Angew. Chem., Int. Ed.*, 2025, **64**, e202505372.
- 54 X. Shi, J. Xie, J. Wang, S. Xie, Z. Yang and X. Lu, *Nat. Commun.*, 2024, **15**, 302.
- 55 X. Yu, M. Chen, Z. Li, X. Tan, H. Zhang, J. Wang, Y. Tang, J. Xu, W. Yin, Y. Yang, D. Chao, F. Wang, Y. Zou, G. Feng, Y. Qiao, H. Zhou and S. G. Sun, *J. Am. Chem. Soc.*, 2024, **146**, 17103–17113.
- 56 J. Lu, T. Wang, J. Yang, X. Shen, H. Pang, B. Sun, G. Wang and C. Wang, *Angew. Chem., Int. Ed.*, 2024, **63**, e202409838.
- 57 D. W. Smith, *J. Chem. Educ.*, 1977, **54**, 540–542.
- 58 Z. X. Zhou, M. M. Han, Y. D. Sun, Y. X. Cui, S. A. El-khodary, D. H. L. Ng, J. B. Lian and J. M. Ma, *Adv. Funct. Mater.*, 2024, **34**, 2308834.
- 59 L. Wang, K. W. Huang, J. Chen and J. Zheng, *Sci. Adv.*, 2019, **5**, eaax4279.
- 60 Z. L. Li, S. Ganapathy, Y. L. Xu, Z. Zhou, M. Sarilar and M. Wagemaker, *Adv. Energy Mater.*, 2019, **9**, 1900237.
- 61 S. Li, C. Huang, L. Gao, Q. Shen, P. Li, X. Qu, L. Jiao and Y. Liu, *Angew. Chem., Int. Ed.*, 2022, **61**, e202211478.
- 62 Y. F. Yuan, R. Sharpe, K. He, C. H. Li, M. T. Saray, T. C. Liu, W. T. Yao, M. Cheng, H. L. Jin, S. Wang, K. Amine, R. Shahbazian-Yassar, M. S. Islam and J. Lu, *Nat. Sustain.*, 2022, **5**, 890–898.
- 63 H. Chen, C. Dai, F. Xiao, Q. Yang, S. Cai, M. Xu, H. J. Fan and S. J. Bao, *Adv. Mater.*, 2022, **34**, e2109092.
- 64 H. L. Pan, Y. Y. Shao, P. F. Yan, Y. W. Cheng, K. S. Han, Z. M. Nie, C. M. Wang, J. H. Yang, X. L. Li, P. Bhattacharya, K. T. Mueller and J. Liu, *Nat. Energy*, 2016, **1**, 16039.
- 65 L. Wang, J. Yan, Y. Hong, Z. Yu, J. Chen and J. Zheng, *Sci. Adv.*, 2023, **9**, eadf4589.
- 66 M. L. Chen, X. He, M. Zhou, J. Ning, Z. D. Zhang, S. L. Cao, T. Q. Wang, K. L. Wang and K. Jiang, *Adv. Energy Mater.*, 2024, **14**, 2400724.
- 67 C. Lee, Y. Hong, D. Kim, Y. Lim, J. W. Choi and S. Y. Chung, *Adv. Funct. Mater.*, 2023, **33**, 2303763.
- 68 Q. Chen, X. Lou, Y. Yuan, K. You, C. Li, C. Jiang, Y. Zeng, S. Zhou, J. Zhang, G. Hou, J. Lu and Y. Tang, *Adv. Mater.*, 2023, **35**, e2306294.
- 69 F. Wang, L. E. Blanc, Q. Li, A. Faraone, X. Ji, H. H. Chen-Mayer, R. L. Paul, J. A. Dura, E. Y. Hu, K. Xu, L. F. Nazar and C. S. Wang, *Adv. Energy Mater.*, 2021, **11**, 2102016.
- 70 S. Deng, H. Li, B. Chen, Z. Xu, Y. Jiang, C. Li, W. Xiao and X. Yan, *Chem. Eng. J.*, 2023, **452**, 139115.
- 71 S. Hou, J. Luo, W. Gong, Y. Xie, X. Zhou, F. Yue, J. Shen, C. Li, L. Wei, F. Xu and Q. Zhang, *ACS Nano*, 2024, **18**, 31524–31536.
- 72 S. Jin, F. Duan, X. Wu, J. Li, X. Dan, X. Yin, K. Zhao, Y. Wei, Y. Sui, F. Du and Y. Wang, *Small*, 2022, **18**, e2205462.
- 73 Q. He, T. Hu, Q. Wu, C. Wang, X. Han, Z. Chen, Y. Zhu, J. Chen, Y. Zhang, L. Shi, X. Wang, Y. Ma and J. Zhao, *Adv. Mater.*, 2024, **36**, e2400888.
- 74 G. Mahendra, R. Roy and A. K. Singh, *J. Power Sources*, 2024, **624**, 235515.
- 75 D. Guo, J. Sun, C. Wang, H. Quan, H. Lu, Y. Wei, C. Sun and S. Wang, *Angew. Chem., Int. Ed.*, 2025, **64**, e202505102.
- 76 J. Li, K. Ge, A. O. Grammenos, P. L. Taberna, P. Simon, M. Antonietti and M. Odziomek, *Adv. Mater.*, 2025, **37**, e2502422.
- 77 Y. H. Dai, R. H. Lu, C. Y. Zhang, J. T. Li, Y. F. Yuan, Y. Mao, C. M. Ye, Z. J. Cai, J. X. Zhu, J. H. Li, R. H. Yu, L. M. Cui, S. Y. Zhao, Q. Y. An, G. J. He, G. I. N. Waterhouse, P. R. Shearing, Y. Ren, J. Lu, K. Amine, Z. Y. Wang and L. Q. Mai, *Nat. Catal.*, 2024, **7**, 776–784.
- 78 J. Wang, X. Gao, Y. Wang, R. Pan, Z. Liu, X. Liu, H. Xie, F. Yu, G. Wang and T. Gu, *Nano Res. Energy*, 2024, **3**, e9120124.

